

## RESEARCH ARTICLE

10.1002/2014GC005641

## Special Section:

The Lithosphere-asthenosphere System

## Key Points:

- Edge-driven convection and shear-driven upwelling can sustain mantle melting
- Such a combination can feed volcanism along the margins of the Colorado Plateau
- Asthenospheric shearing and viscosity heterogeneity are sufficient for magmatism

## Supporting Information:

- Readme
- Movie S1
- Movie S2

## Correspondence to:

M. D. Ballmer,  
ballmer@elsi.jp

## Citation:

Ballmer, M. D., C. P. Conrad, E. I. Smith, and R. Johnsen (2015), Intraplate volcanism at the edges of the Colorado Plateau sustained by a combination of triggered edge-driven convection and shear-driven upwelling, *Geochem. Geophys. Geosyst.*, 16, 366–379, doi:10.1002/2014GC005641.

Received 4 NOV 2014

Accepted 14 JAN 2015

Accepted article online 20 JAN 2015

Published online 5 FEB 2015

## Intraplate volcanism at the edges of the Colorado Plateau sustained by a combination of triggered edge-driven convection and shear-driven upwelling

Maxim D. Ballmer<sup>1,2</sup>, Clinton P. Conrad<sup>1</sup>, Eugene I. Smith<sup>3</sup>, and Racheal Johnsen<sup>3</sup>

<sup>1</sup>Department of Geology and Geophysics, School of Ocean and Earth Sciences and Technology, University of Hawaii at Manoa, Honolulu, Hawaii, USA, <sup>2</sup>Earth-Life Science Institute, Tokyo Institute of Technology, Meguro, Tokyo, Japan, <sup>3</sup>Department of Geoscience, University of Nevada Las Vegas, Las Vegas, Nevada, USA

**Abstract** Although volcanism in the southwestern United States has been studied extensively, its origin remains controversial. Various mechanisms such as mantle plumes, upwelling in response to slab sinking, and small-scale convective processes have been proposed, but have not been evaluated within the context of rapidly shearing asthenosphere that is thought to underlie this region. Using geodynamic models that include this shear, we here explore spatiotemporal patterns of mantle melting and volcanism near the Colorado Plateau. We show that the presence of viscosity heterogeneity within an environment of asthenospheric shearing can give rise to decompression melting along the margins of the Colorado Plateau. Our models indicate that eastward shear flow can advect pockets of anomalously low viscosity toward the edges of thickened lithosphere beneath the plateau, where they can induce decompression melting in two ways. First, the arrival of the pockets critically changes the effective viscosity near the plateau to trigger small-scale edge-driven convection. Second, they can excite shear-driven upwelling (SDU), in which horizontal shear flow becomes redirected upward as it is focused within the low-viscosity pocket. We find that a combination of “triggered” edge-driven convection and SDU can explain volcanism along the margins of the Colorado Plateau, its encroachment toward the plateau’s southwestern edge, and the association of volcanism with slow seismic anomalies in the asthenosphere. Geographic patterns of intraplate volcanism in regions of vigorous asthenospheric shearing may thus directly mirror viscosity heterogeneity of the sublithospheric mantle.

### 1. Introduction

Whereas volcanism along mid-ocean ridges and subduction zones primarily reflects plate-tectonic processes, the study of intraplate volcanism can reveal mantle flow and composition. Volcanism in the western United States has been the target of many studies that utilize geophysical, geochemical, and geological constraints, but its origin remains controversial. Proposed mechanisms for volcanism include mantle plumes [Camp and Ross, 2004; Smith *et al.*, 2009; Obrebski *et al.*, 2010], lithospheric deformation [e.g., Valentine and Hirano, 2010], return flow due to lithospheric dripping [Le Pourhiet *et al.*, 2006; Gogus and Pysklywec, 2008; West *et al.*, 2009; Levander *et al.*, 2011; Reid *et al.*, 2012] or in response to slab sinking [Liu and Stegman, 2012], buoyant decompression melting [Hernlund *et al.*, 2008], as well as edge-driven convection [van Wijk *et al.*, 2008, 2010]. Most of these mechanisms exploit mantle density variations as the main energy source for mantle upwelling and decompression melting. However, they ignore the presence of horizontal shearing of the asthenosphere (Figure 1), which is as vigorous, or more so, beneath the western United States compared to any other continental environment on Earth [Conrad *et al.*, 2011].

Recent work shows that, in the presence of ample viscosity heterogeneity (i.e., viscosity contrasts of about one order of magnitude or more) and/or sublithospheric topography ( $\geq 10$  km), vigorous asthenospheric shearing is sufficient to generate mantle upwelling and decompression melting, and lateral density variations are not required [Conrad *et al.*, 2010]. For example, horizontal shear flow is redirected into up or downwellings at steps of lithospheric thickness (Figure 2a) as associated with rifts or the keels of cratons and continental plateaus [e.g., Harig *et al.*, 2010]. Also, focusing and defocusing of shear flow at the margins of “pockets” of anomalously low viscosity asthenosphere is compensated by localized up and downwellings

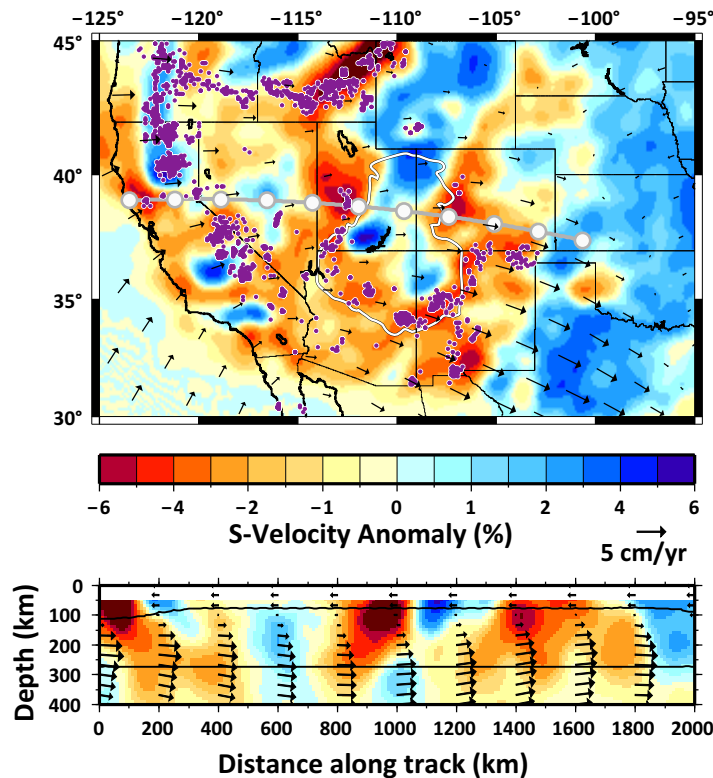


**Figure 1.** Basaltic volcanism, shear-wave velocities (anomalies relative to AK135 from Schmandt and Humphreys [2010]; colors) and mantle flow (from global flow model of Conrad and Behn [2010]; arrows) in the western United States. (top) A horizontal cross section of seismic shear-wave tomography and of mantle flow at 160 km depth. Map view of recent basaltic volcanism ( $\leq 5$  Ma and  $\leq 58\%$  SiO<sub>2</sub> from NAVDAT; purple dots) and the outline of the Colorado Plateau (white line) are superimposed. In addition to Yellowstone, the Snake River Plain, the High Lava Plains, and the Sierra Nevada, basaltic volcanism is focused along three out of four edges of the Colorado Plateau, which coincide with slow velocities in the mantle. (bottom) Vertical cross section of mantle flow (black lines are asthenospheric bounds) and shear-wave velocity anomalies along the gray profile (see top plot). Gray circles along the profile are spaced 200 km.

(Figure 2b). Both styles of shear-driven upwelling (SDU) can give rise to decompression melting with specific geographical patterns of volcanism, provided the asthenosphere is initially close to its solidus [Bianco *et al.*, 2011; Ballmer *et al.*, 2013a]. Conrad *et al.* [2011] find that continental intraplate volcanism indeed occurs more frequently where asthenospheric shearing is vigorous.

Geophysical observations indicate that all three requirements for SDU – (1) sublithospheric topography and/or viscosity heterogeneity, (2) near-solidus mantle, and (3) shear flow – are present beneath the western United States. For example, the Colorado Plateau is supported by a lithospheric keel  $\sim 110$  km thick with sharp steps in lithospheric thickness (40–60 km high) [Levander and Miller, 2012] along its margins, where recent volcanism is concentrated (Figure 1). Basin and Range (and Rio Grande Rift) lithosphere juxtaposed to the Colorado Plateau is relatively thin due to extension and modification by Farallon-slab-

derived fluids [Sonder and Jones, 1999; Humphreys *et al.*, 2003; Levander and Miller, 2012]. Regional seismic tomography studies moreover image localized low-velocity anomalies along the margins of the plateau [e.g., Obrebski *et al.*, 2010; Schmandt and Humphreys, 2010], providing evidence for low-viscosity material

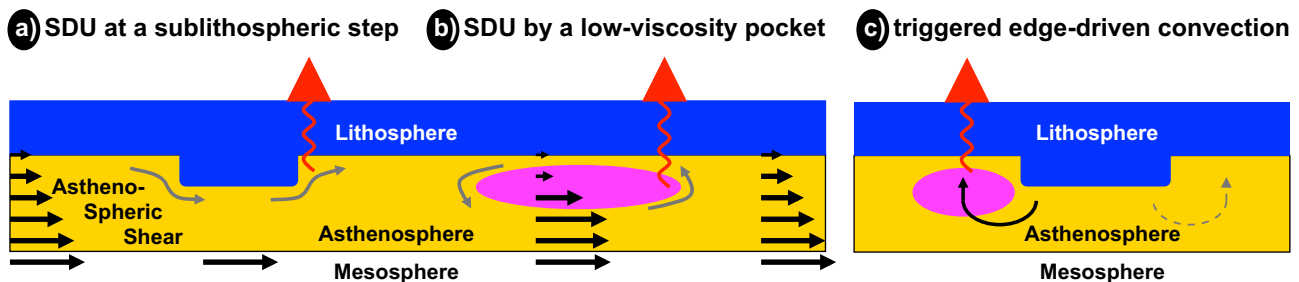


**Figure 2.** Two-dimensional cartoons of shear-driven upwelling (SDU) and triggered edge-driven convection (TEDC). Black horizontal arrows show vertical profiles of shear flow in the asthenosphere (yellow) in response to relative motion between the lithosphere (blue) and mesosphere. (a) Shear flow is redirected along the base of thickened lithosphere (gray arrows) with opportunities for volcanism above resulting upwellings (red). (b) Vertical flow alternatively arises from redistribution of shear flow at the edges of a low-viscosity pocket (magenta). This redistribution is due to the preferential relaxation of shear across the pocket. Note the difference in vertical profiles of shear flow across the pocket (center) and across the ambient mantle (left and right). Finally, (c) edge-driven convection is driven by lateral density differences between thickened lithosphere and asthenosphere, independent of horizontal shear flow in the mantle. The presence of a low-viscosity pocket is required to trigger vigorous edge-driven convection and magmatism.

**Table 1.** Notations

Parameter	Symbol	Value
Adiabatic gradient	$\gamma$	0.38882 K/km
Latent heat of melt	$L$	560 kJ/kg
Activation energy <sup>a,c</sup>	$E^*$	200 kJ/mol
Activation volume	$V^*$	$5 \times 10^{-6} \text{ m}^3/\text{mol}$
Reference mantle viscosity	$\eta_0$	$5.894\text{--}10.72 \times 10^{18} \text{ Pa}\cdot\text{s}$
Effective mantle viscosity	$\eta_m$	$0.3\text{--}15 \times 10^{18} \text{ Pa}\cdot\text{s}^f$
Effective pocket viscosity	$\eta_p$	$15\text{--}27.3 \times 10^{18} \text{ Pa}\cdot\text{s}^f$
Reference temperature	$T_m$	1350 °C
Mantle density	$\rho_m$	3300 kg/m <sup>3</sup>
Melt extraction threshold	$\varphi_C$	0.1%
Dehydration stiffening coefficient <sup>d</sup>	$\xi$	100
Melt lubrication exponent <sup>e</sup>	$\zeta$	-40
Thermal expansivity	$\alpha$	$3 \times 10^{-5} \text{ K}^{-1}$
Crustal radiogenic heat production rate	$Q_{\text{Rth}}$	$7 \times 10^{-10} \text{ W/kg}$
Water partitioning coefficient	$D_{\text{H}_2\text{O}}$	0.01
Bottom velocity boundary condition	$v_{\text{bottom}}$	5 cm/yr
Bulk water content in the ambient mantle	$c_{0,m}$	20.95–26.25 wt.-ppm <sup>f</sup>
Bulk pocket water content	$c_{0,p}$	731.1 wt.-ppm
Water content at which peridotite behaves like dry Peridotite	$c_{\text{dry}}$	6 wt.-ppm
Ideal gas constant	$R$	8.31446 J·mol <sup>-1</sup> ·K <sup>-1</sup>
Gravity acceleration	$g$	9.8 m/s <sup>2</sup>

<sup>a</sup>Activation energy is adjusted to mimic the effects of deformation by dislocation creep [Christensen, 1984].

<sup>b</sup>Karato and Wu [1993].

<sup>c</sup>Hirth [2002].

<sup>d</sup>Hirth and Kohlstedt [1996].

<sup>e</sup>Kohlstedt and Zimmerman [1996].

<sup>f</sup>See also Table 2.

sustained by high temperature, volatile content, melt, or a combination thereof. In addition to seismic constraints, high heat flow [Blackwell and Richards, 2004] and widespread volcanism indicates that the mantle is close to or at its solidus. Finally, geodynamic models constrained by plate motions and mantle seismic wave speed variations predict eastward to NE ward flow at the base of the asthenosphere by rates of ~5 cm/yr relative to the North American plate [Becker, 2006; Forte et al., 2007, 2010a; Conrad and Behn, 2010; see also West et al., 2009]. The resulting asthenospheric shearing, which is driven by the descent of the Farallon slab beneath eastern North America, is consistent with observations of seismic anisotropy beneath the western United States [Becker et al., 2006; Beghein et al., 2010; Yuan and Romanowicz, 2010].

The tectonic setting of the Colorado Plateau also offers the proper conditions for another geodynamic mechanism for decompression melting. Edge-driven convection may be occurring along steps of lithospheric thickness [King and Anderson,

1998; Huang et al., 2003; Kaislaniemi and van Hunen, 2014], where cold and dense sublithospheric mantle is juxtaposed to warm and buoyant asthenosphere. Volcanism and recent uplift occurring along the edges of the Colorado Plateau have indeed been ascribed to this mechanism [van Wijk et al., 2010]. Except for a recent study on the origin of volcanism in SE Australia [Davies and Rawlinson, 2014], the effects of asthenospheric shear flow on edge-driven convection have so far only been studied in simple two-dimensional settings [e.g., Till et al., 2010], and the additional influence of viscosity heterogeneity within the shearing asthenosphere has been neglected altogether.

Here, we use three-dimensional numerical models of mantle flow and melting to investigate the spatiotemporal patterns of melting near the Colorado Plateau. We characterize the roles of asthenospheric shearing, viscosity heterogeneity, and sublithospheric topography on mantle flow in order to explore the interaction of SDU and edge-driven convection. Finally, we assess which of these two mechanisms dominantly feeds magmatism, and discuss the origin of viscosity heterogeneity beneath the southwestern United States, which we find to be critical for magmatism.

## 2. Methods

We model mantle flow using the numerical code CITCOM [Moresi et al., 1996; Zhong et al., 2000]. In solving the equations of conservation of mass, momentum and energy, we apply the Boussinesq approximations, and additionally account for the effects of adiabatic heating and latent heat of melting (for a list of governing parameters, see Table 1). Passive tracers are used to advect nondiffusive fields (i.e., composition). The model domain is a rectangular box 2910 km long, 540 km wide and 300 km deep, discretized by 960×192×96 finite elements with a maximal resolution of 2.81×2.68×2.37 km<sup>3</sup> in the asthenosphere. The modeled fluid is cooled from above and heated from below. We impose a boundary condition of  $v_{\text{bottom}} = 5 \text{ cm/yr}$  at the base of the box to simulate mantle motion relative to the North American Plate. Both the front and back sides of the box are open to in and outflow, whereas the bottom is closed. The lateral sides are reflective boundaries, a setup that effectively doubles the width of the model domain to

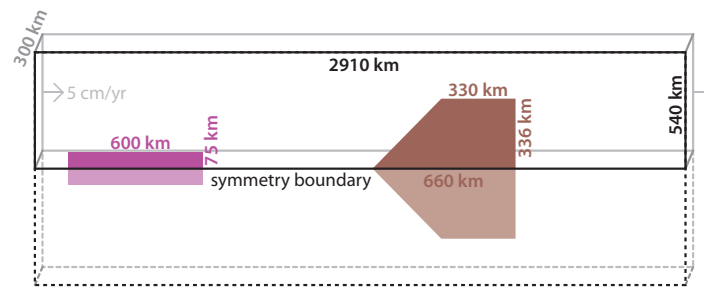


**Figure 3.** Overview of the three-dimensional model setup in a view from above. Brown and purple colors show surface projections of the initial positions of the plateau's keel and low-velocity pocket, respectively. In some cases, the pocket is centered at the symmetry boundary at  $y = 0$  (as shown), in others it is displaced from it (not shown); cf. Table 2. A bottom velocity boundary condition drives flow into and out of the box (arrows), as well as asthenospheric shearing. The dashed and shaded domain beyond the symmetry boundary is not modeled explicitly, but instead results from symmetry about the reflecting side boundaries.

1080 km (Figure 3) with a symmetry axis along the central plane of the box at  $y = 0$  (and parallel to vector  $v_{bottom}$ ).

Initial conditions include a region of thickened lithosphere centered along this central plane with a pentagonal "home plate" shape (for geometry, see Figure 3) and dimensions similar to those of the Colorado Plateau (Figure 1). Initial water content  $c$  of the lithosphere is calculated from a melting column residual depletion profile [Ballmer *et al.*, 2009]

with a depleted top layer of thickness 30 km added to the profile in the region of the plateau. Initial temperatures correspond to a 30 Myr half-space cooling profile in this region, and a 5 Myr half-space cooling profile elsewhere, but quickly evolve during the simulations due to thermal conduction. In order to limit conductive thickening of the continental lithosphere, we also account for radiogenic heating. At depths of  $<60$  km and  $<30$  km inside and outside the plateau region, respectively, the lithosphere is heated at rates  $Q_{lith}$ . The plateau's edges are relatively sharp with slopes of  $\sim 63^\circ$ .

We further impose a rectangular low-viscosity pocket 600 km long, 75 km wide (which becomes doubled by the model symmetry; Figure 3), and 90 km high. The possible widths and heights of the pocket are limited in our model setup, as flow within pockets that are much smaller than those modeled would be underresolved. The initial average depth of the pocket  $z_p$  is varied as a function of effective mantle viscosity  $\eta_m$  (for a list of all cases, see Table 2), such that the average depth of the pocket at model time  $\sim 25$  Myr (i.e., when the slowly ascending pocket reaches the plateau's edge) is similar in all cases (i.e.,  $z_{edge} \approx 137.5$  km). We are able to choose an appropriate value of  $z_p$  because the pocket's rise rate is consistent with Stokes Law, that is  $z_p - z_{edge} \sim 1/\eta_m$ . In some cases, the pocket is centered at the symmetry plane of the box ( $y_p = 0$ ) such that one wide pocket (of effective width 150 km) is simulated; in others, it is laterally displaced such that two pockets (each 75 km wide, mirrored by the symmetry plane) are effectively modeled. In the direction of  $v_{bottom}$ , the pocket center is initially positioned 1050 km away from the plateau's edge, which, because of the shape of the plateau, requires that the pocket's distance from the inflow boundary be varied as a function of  $y_p$ . The viscosity contrast between the pocket and the ambient mantle  $\eta_m/\eta_p$  is sustained by a combination of slightly elevated pocket temperatures ( $+10^\circ\text{C}$ ) and significantly elevated pocket water contents  $c_{0,p}$  (731.1 wt.-ppm compared to  $c_{0,m} < 27$  wt.-ppm in the ambient mantle). The warm and damp anomaly is a step function smoothed over a buffer 12 km thick. We vary  $\eta_m/\eta_p$  between 37.5 and 50 and adjust  $c_{0,m}$  accordingly (see Table 2). We adjust  $c_{0,m}$  instead of  $c_{0,p}$  in order to keep the melting behavior of the material in the pocket fixed between cases. In varying  $c_{0,m}$  (and thus  $\eta_m/\eta_p$ ), we further adjust the reference mantle viscosity  $\eta_0$  to keep  $\eta_m$  (and thus the vigor of mantle convection) fixed.

Density and viscosity variations control mantle flow. In order to focus on shear-driven flow and its relationship to thermally driven convection, density  $\rho$  in our models is assumed to depend on temperature  $T$  only:  $\rho = \rho_m + \alpha(T_m - T)$ . In contrast, mantle viscosity  $\eta$  in our models depends on both temperature and composition (for notations, see Table 1). Retained melt lubricates mantle rocks [Kohlstedt and Zimmerman, 1996], but stiffening due to dehydration during progressive melting is dominant according to our parameterization [cf. Karato, 1986]. Peridotites dehydrate as depletion  $F$  increases during melt production (we use Katz *et al.*'s [2003] parameterization to model mantle melting) and extraction:

$$c = \frac{D_{H_2O} c_0}{F + D_{H_2O}(1 - F)} \quad (1)$$

for  $F < \varphi_G$  and

**Table 2.** Model Cases With Key Parameters

Case	$\eta_m/\eta_p$	$\eta_p$ (Pa s)	$\eta_m$ (Pa s)	$c_{0,p}$ (ppm)	$y_p$ (km)	$z_p$ (km)	Pocket Width (km)
A	50	$0.3 \times 10^{18}$	$1.5 \times 10^{19}$	20.95	0	180	75
B	50	$0.3 \times 10^{18}$	$1.5 \times 10^{19}$	20.95	97.5	180	75
C	50	$0.3 \times 10^{18}$	$1.5 \times 10^{19}$	20.95	157.5	180	75
D	50	$0.3 \times 10^{18}$	$1.5 \times 10^{19}$	20.95	217.5	180	75
E	50	$0.3 \times 10^{18}$	$1.5 \times 10^{19}$	20.95	277.5	180	75
F	50	$0.3 \times 10^{18}$	$1.5 \times 10^{19}$	20.95	337.5	180	75
A1	50	$0.34 \times 10^{18}$	$1.7 \times 10^{19}$	20.95	0	175	75
E1	50	$0.34 \times 10^{18}$	$1.7 \times 10^{19}$	20.95	277.5	175	75
A2	50	$0.4 \times 10^{18}$	$2 \times 10^{19}$	20.95	0	169.2	75
E2	50	$0.4 \times 10^{18}$	$2 \times 10^{19}$	20.95	277.5	169.2	75
A2'	44.118	$0.4 \times 10^{18}$	$1.765 \times 10^{19}$	23.07	0	175	75
E2'	44.118	$0.4 \times 10^{18}$	$1.765 \times 10^{19}$	23.07	277.5	175	75
A2''	37.5	$0.4 \times 10^{18}$	$1.5 \times 10^{19}$	26.25	0	180	75
E2''	37.5	$0.4 \times 10^{18}$	$1.5 \times 10^{19}$	26.25	277.5	180	75
A3	50	$0.545 \times 10^{18}$	$2.73 \times 10^{19}$	20.95	0	160.8	75
E3	50	$0.545 \times 10^{18}$	$2.73 \times 10^{19}$	20.95	277.5	160.8	75
An	1 <sup>a</sup>	$1.5^a \times 10^{19}$	$1.5 \times 10^{19}$	20.95	0	180	75
En	1 <sup>a</sup>	$1.5^a \times 10^{19}$	$1.5 \times 10^{19}$	20.95	277.5	180	75
N	1	no pocket	$1.5 \times 10^{19}$	20.95	N/A	N/A	0

<sup>a</sup>In cases An and En, the viscosity of the pocket is artificially increased to match that of the surrounding mantle, but the melting behavior of the pocket material is analogous to all other cases (except case N), in which pocket water content  $c_{0,p}$  is fixed at 731.1 wt.-ppm. The purpose of cases A–F is to study the effect of pocket initial position. The purpose of cases An and En is to test the effect of an absence of a low-viscosity pocket. Case N is a reference case without a pocket, the predictions of which are used for the subtraction of background shear flow in Figures 4 and 6. The purpose of all other cases is to explore the effects of mantle rheology.

$$c = c_0 \left( \left( 1 - \frac{F - \varphi_c}{1 - \varphi_c} \right)^{\frac{1}{\varphi_c(1 - D_{H2O}) + D_{H2O}}} - 1 \right) \left( 1 + \varphi_c \left( \frac{1}{D_{H2O}} - 1 \right) \right)^{-1} \quad (2)$$

for  $F \geq \varphi_c$  [Zou, 1998; Ballmer et al., 2013b] with  $\varphi_c = 0.1\%$  the critical porosity, at which melt is mobilized (all notations are reported in Table 1). Accordingly, mantle viscosity is a function of depletion  $F$  (substituting Eq. (1) and/or Eq. (2) into Eq. (3)) and melt content  $\varphi$ , in addition to temperature  $T$  and depth  $z$ :

$$\eta = \eta_0 \exp \left( \frac{E^* + \rho_m g z V^*}{RT} - \frac{E^*}{RT_m} \right) \frac{\zeta(c - c_{dry})}{(\zeta - 1) \exp(\zeta_\varphi)} \quad (3)$$

### 3. Results

In our models, a rectangular low-viscosity pocket is initially positioned 1050 km away from (i.e., west of) the edge of the Colorado Plateau. It is entrained and deformed by eastward asthenospheric shear flow and advected toward the plateau. Asthenospheric shearing is preferentially released across the pocket of low viscosity. Focusing and defocusing of shear flow leads to localized up and downwellings at the leading and trailing edges of the pocket, respectively. Such a redirection of horizontal into vertical motion by the presence of a low-viscosity pocket is analogous, but opposite, to the rotation of a stiff inclusion (such as a garnet within a sheared quartz package). This “shear-driven upwelling” (SDU) is artificially vigorous for rectangular pocket geometries, but persists for more realistic geometries that have been shaped by mantle flow. In addition, a small thermal anomaly assigned to the pocket (+10 °C) causes slow ascent of the pocket as a whole. These two mechanisms initially sustain decompression melting in the pocket (Figure 4a). However, the initial large vigor of melting declines as soon as the pocket reaches the base of the lithosphere and takes a nonrectangular geometry (Figure 4b). Small-extent melting continues as the pocket travels along the base of the lithosphere and may be applicable to Basin and Range volcanism. Melting rates steadily decrease with distance traveled, however, and are only boosted as the pocket reaches the plateau.

The interaction of the pocket with the plateau’s thick lithospheric keel depends on the initial position of the pocket relative to that of the plateau. In cases A–F, we vary the initial distance of the pocket center relative to the symmetry plane of the model (and of the plateau)  $y_p$ . For cases with  $y_p \leq 180$  km (cases A–C), the pocket tunnels beneath the plateau’s keel, which plows through the asthenosphere to redirect shear flow.

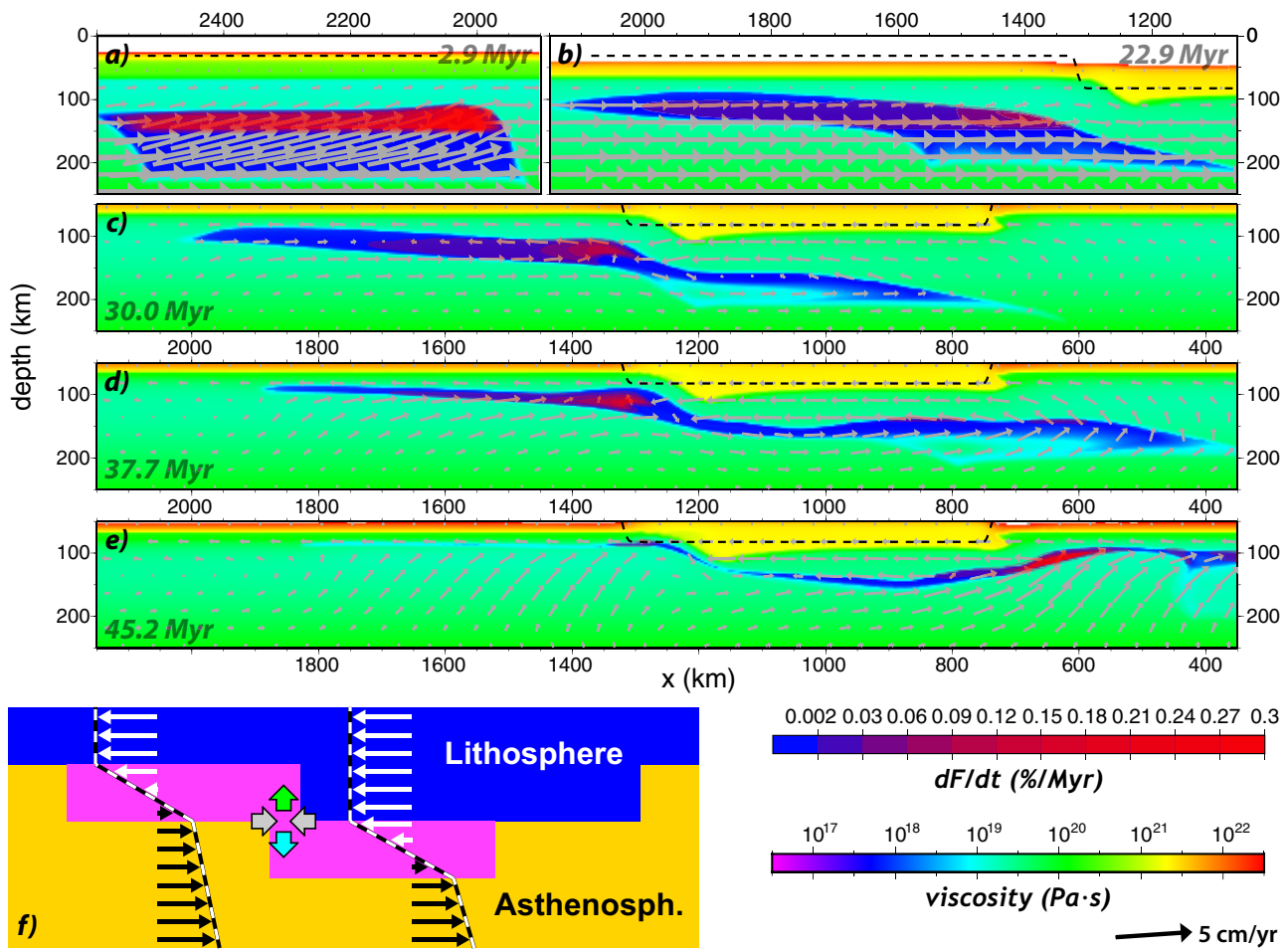


**Figure 4.** (a–e) Time series of melting in a low-viscosity pocket (deep blue) that tunnels beneath a plateau’s lithospheric keel (yellow). Results are from case B. Rainbow colors show mantle viscosity in vertical cross sections parallel to plate motion at  $y = 100$  km. Dashed black lines denote the initial shape of the lithosphere–asthenosphere boundary; the current shape is marked by the transition from yellow to green colors. Melting in the low-viscosity pocket is shaded translucent red. Arrows denote mantle flow with (Figures 4c–4e) and without (Figures 4a–4b) background shear flow subtracted. Also note that the scales are shifting between Figures 4a and 4b and Figures 4c–4e, as the pocket is approaching the plateau. Initial vigorous melting is an artefact of the model setup (Figure 4a; see text), declines before the pocket arrives at the edge of the plateau (Figure 4b), and is reinvigorated due to plateau–pocket interaction (Figures 4c–4e). (f) Conceptual cartoon of SDU at the leading edge of a plateau such as in Figures 4c and 4d. Black and white arrows show vertical profiles of horizontal shear flow relative to the pocket. Shear is preferentially relaxed across each of the two subpockets of low viscosity (magenta). The resulting convergence at the leading edge of the plateau’s keel (gray arrows) induces vertical flow (colored arrows) and decompression melting in front of the plateau.

For cases with  $y_p \geq 180$  km (cases D–F), the pocket is instead guided around the nearest side of the plateau without significant vertical motion.

### 3.1. Example Case B: Pocket Traveling Beneath the Keel

For example in case B ( $y_p = 97.5$  km), the pocket is drawn beneath the plateau’s keel as soon as it reaches the plateau (Figure 4). Although it is drawn downward as a whole, a component of vigorous upwelling persists within the pocket near the leading edge of the plateau. This upwelling is fueled by two different mechanisms.

First, small-scale convection at the plateau’s edge is triggered by the presence of the low-viscosity pocket. The arrival of the pocket increases the local Rayleigh number near the plateau (i.e., decreases local viscosity), which leads to the onset of edge-driven convection. We refer to this convection style as “triggered” edge-driven convection (TEDC, Figure 2c). While TEDC downwelling occurs inboard of the plateau’s edge, TEDC upwelling occurs parallel to and  $\sim 100$  km in front (i.e., west) of the plateau. Flow related to TEDC is superimposed on background shear flow. Such a superposition precludes the development of proper convection rolls in front of the plateau, but does not remove the upwelling (and downwelling) flow components that

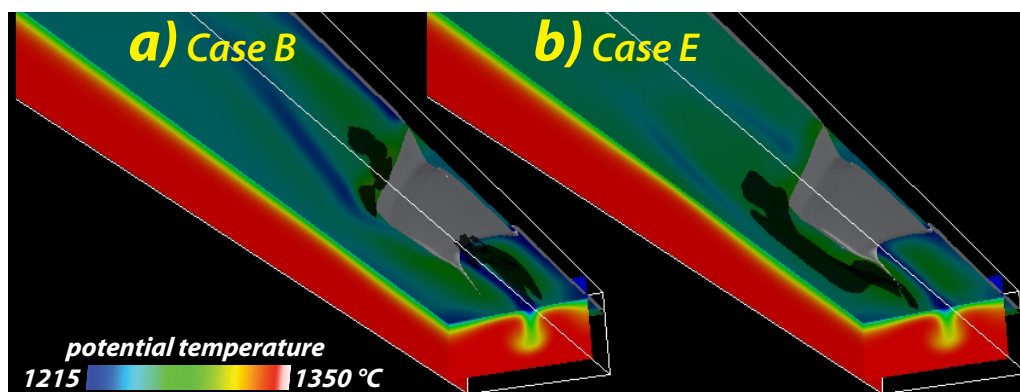


**Figure 5.** Snapshots (after 43 Myr model time) of mantle temperatures and decompression melting (translucent black) within a low-velocity pocket (not shown) in three-dimensional views looking up at the front edge and base of the plateau keel (denoted in gray) from below. Potential temperatures (i.e., temperatures corrected for adiabatic heating) are shown as rainbow colors along horizontal and vertical cross sections. (a) Melting occurs upstream (left) and downstream (right) of the plateau in case B, and (b) mainly alongside of the plateau's sides in case E. See also supporting information Movies S1 (Figure 5a) and S2 (Figure 5b).

are related to TEDC (Figure 4c). In contrast to “standard” edge-driven convection [King and Anderson, 1998], vigorous TEDC requires not only a step in lithospheric thickness but also the presence of a low-viscosity pocket.

Second, SDU is reinvigorated as the pocket is partially drawn beneath the plateau's keel, and thereby subdivided into two subpockets. While the lower part of the pocket slides beneath the plateau's keel, the upper part remains trapped in front. SDU develops in both subpockets. A local dynamic pressure maximum due to convergent horizontal flow explains the increased vigor of SDU in front of the plateau where both subpockets meet (Figures 4c and 4d). This convergent flow is a direct consequence of shear partitioning across an asthenosphere, in which a step of lithospheric thickness is juxtaposed with two low-viscosity subpockets that preferentially accommodate shear (see cartoon in Figure 4f).

The presence of the low-viscosity pocket plays an important role for sustaining upwelling and generating mantle melting via both TEDC and SDU. In our models, edge-driven convection is much weaker and insufficient for decompression melting until the low-viscosity pocket arrives. Moreover, shear-driven flow becomes redirected by the leading edge of a region of thick lithosphere into upwelling (not downwelling, as would be expected without the presence of viscosity heterogeneity (Figure 2a)). This is demonstrated by cases in which we artificially increase the viscosity of the pocket but keep its melting behavior unchanged (cases An and En). In these cases, mantle melting near the plateau is completely shut off.

Figure 5a shows in a three-dimensional snapshot of melting in the pocket for case B that magmatism occurs in front of the plateau and beyond its far side. In contrast, it is shut off as the pocket tunnels beneath the plateau's keel, where pressures exceed those of the solidus for hydrous peridotite. As the lower subpocket reaches the far side (i.e., east side) of the plateau, however, it reascends and decompression melting resumes (Figure 4e). Upwelling on the far side is sustained by a combination of both types of SDU (Figures 2a and 2b), as well as TEDC (Figure 2c). Accordingly, it is more vigorous than in front of the plateau. This vigorous upwelling in combination with a fertile source (the lower subpocket has not experienced previous melting) explains the large extents of melting on the far side.

### 3.2. Example Case E: Pocket Traveling Around the Keel

In contrast to case B (with  $y_p = 97.5$  km), where the pocket tunnels beneath the plateau's keel, the pocket is guided around the plateau in case E ( $y_p = 277.5$  km). Only part of the pocket is intermittently trapped at the plateau's leading corners to induce localized magmatism (Figures 6a and 6b) in a similar manner as described above (cf. Figure 4f). As soon as the pocket moves alongside the plateau's flanks (i.e., adjacent to the southern and/or northern edges; Figure 5b), however, vigorous and persistent upwelling as well as decompression melting occur. Here, upwelling is sustained by a combination of TEDC and SDU (Figures 6c and 6d), as conditions are favorable for both types of upwelling. TEDC is boosted by the arrival of the low-viscosity pocket causes the entire length of the plateau's edge to become convectively unstable at once.

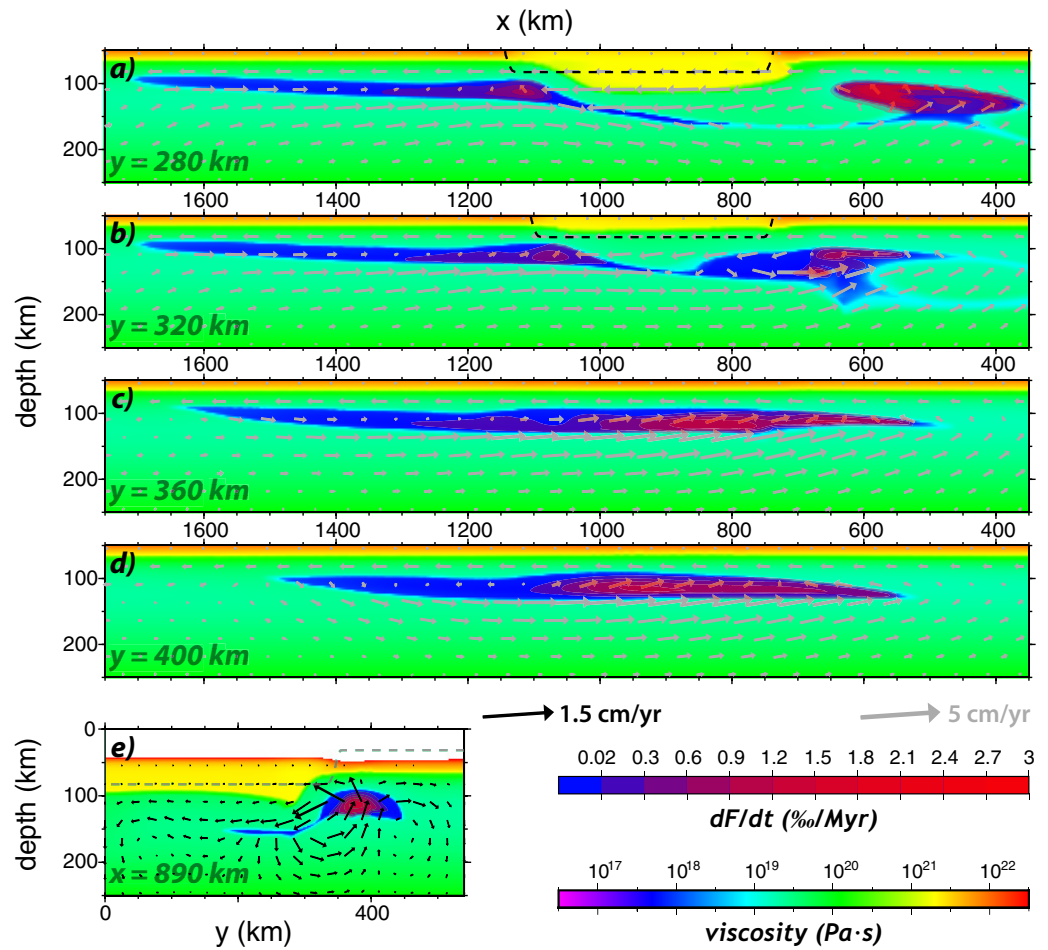


**Figure 6.** Mantle melting at model time 40 Myr in a low-viscosity pocket (deep blue) that travels around the plateau’s lithospheric keel (yellow). Results are represented along (a–d) four vertical cross sections parallel to plate motion and (e) one cross section perpendicular to plate motion through the three-dimensional model of case E. Rainbow colors denote mantle viscosity. Dashed lines denote the initial shape of the lithosphere-asthenosphere boundary; the current shape is marked by the transition from yellow to green colors. Melting in the low-viscosity pocket is shaded translucent red. Arrows show mantle flow with background shear flow subtracted. Vigorous melting occurs as the pocket moves along the east-west length of the plateau (Figures 6c–6e), and tunnels beneath the plateau’s front corner (Figures 6a and 6b).

The resulting edge-parallel upwelling feeds a convective roll that aligns with asthenospheric shear (Figure 6e), a configuration that minimizes interference between background shear flow and TEDC [cf. Richter and Parsons, 1975]. SDU is also somewhat boosted as shear flow becomes concentrated by the presence of the plateau’s keel, which acts to reduce the cross-sectional area of the asthenospheric channel. On the far (eastern) side of the plateau, the pocket is pulled back toward the centerline of the model and also upward by large-scale background shear flow. Here decompression melting occurs as the originally deepest (i.e., previously unmelted) parts of the pocket are brought toward the surface (Figure 6a).

### 3.3. Patterns of Volcanism

The patterns of mantle flow and magmatism in cases A–F define the spatiotemporal trends of associated volcanism. We assume that partial melt in the mantle exceeding 0.1% is instantaneously extracted from the source. Maximum extents of pocket melting remain low (<2%) and are hence insufficient to significantly dehydrate and stiffen the low-viscosity pocket. Figures 7a–7f and 8a–8f show the predicted progressions and cumulative volumes of volcanism for cases A–F, respectively. Cases in which the pocket tunnels beneath the plateau (i.e., cases A–C), display persistent (~20 Myr) volcanism near the (western) leading edge of the plateau and more vigorous (~10 Myr), volcanism near the opposite edge. Cases in which the pocket travels around the plateau (cases D–F), instead display most vigorous volcanism

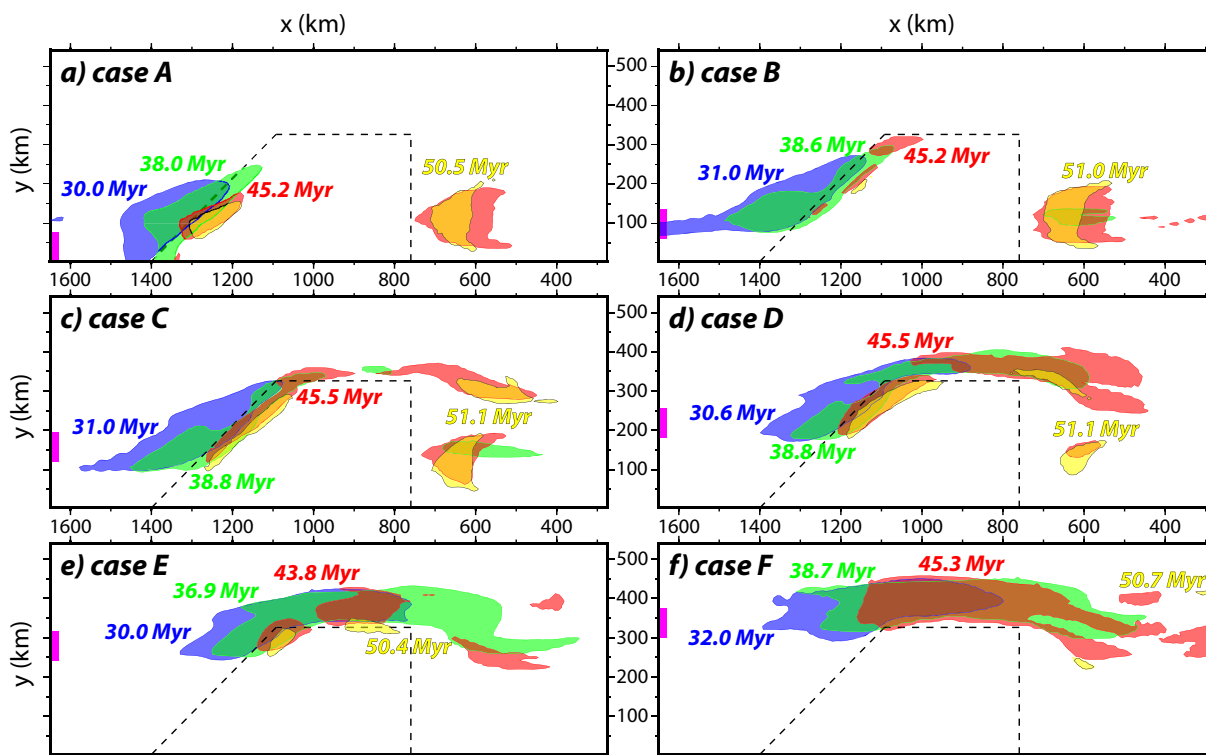


**Figure 7.** Geographical patterns of volcanism predicted by the numerical models (cases A–F) in time series from ~30 Myr to ~50 Myr (time color coded). Volcanism mostly occurs off of the leading and trailing edges of the plateau (cases A–D), and also along the lateral sides (cases D–F), depending on the impact location of the pocket into the plateau (initial  $y$  position of the pocket for each case is shown by pink bar on left). Volcanism occurring off of the leading edge is most persistent and slowly encroaches toward the plateau (blue-to-green-to-red-to-yellow colors).

along the flanks of the plateau. Volcanism occurring at the leading edge or corner(s) of the plateau in cases A–E steadily encroaches toward the plateau at rates of up to 3 km/Myr (Figures 7a–7e). This prediction is consistent with general geographical patterns of Neogene volcanism near the Colorado Plateau, which statistically advances toward the plateau at similar rates [Roy *et al.*, 2009; Crow *et al.*, 2011]. Volcanic encroachment is best documented along the southwestern edge of the Colorado Plateau [Crow *et al.*, 2011, Figure 4], which faces asthenospheric shear flow (Figure 1). The predicted total volumes of magmatism are small ( $<1000 \text{ km}^3/\text{Myr}$  integrated over the whole region), also consistent with observations [Best *et al.*, 1980; Nelson and Tingey, 1997; Johnsen *et al.*, 2010]. For example, Neogene volcanic fluxes (per area) across the Marysvale volcanic field (SW Utah) of  $\sim 4 \text{ m}/\text{Myr}$  [Rowley *et al.*, 1997] are similar to model predictions of peak magmatic fluxes at the plateau margin for cases A–F ( $\sim 9$  to  $\sim 19 \text{ m}/\text{Myr}$ ; from Figure 8). Because intrusive magmatism and underplating should prevent some magma from erupting, predicted volcanic fluxes remain upper bounds.

Our analysis of cases A–F shows that volcanic patterns strongly depend on the initial position of the pocket relative to the plateau. As multiple low-viscosity pockets may reside in the asthenosphere beneath the western United States, and as their locations and sizes (and trajectories in particular) are poorly constrained, comparison of model predictions with observations is not straightforward. Time-integrated patterns strongly depend on initial pocket position (Figure 8). In an attempt to circumvent this issue, we compute cumulative volcanic fluxes averaged over cases A through F (Figures 8a–8f). Such an analysis elucidates that volcanism due to a combination of SDU and TEDC should generally occur along the edges (i.e., outboard) of the Colorado Plateau (Figure 8g). This prediction is robust and consistent with observations.

### 3.4. Effects of Rheology on Flow and Volcanism

Since both SDU and TEDC are sensitive to lateral changes in mantle viscosity, we systematically explore the effects of pocket viscosity  $\eta_p$  and ambient-mantle viscosity  $\eta_m$  on upwelling and volcanism. We varied  $\eta_m$  as

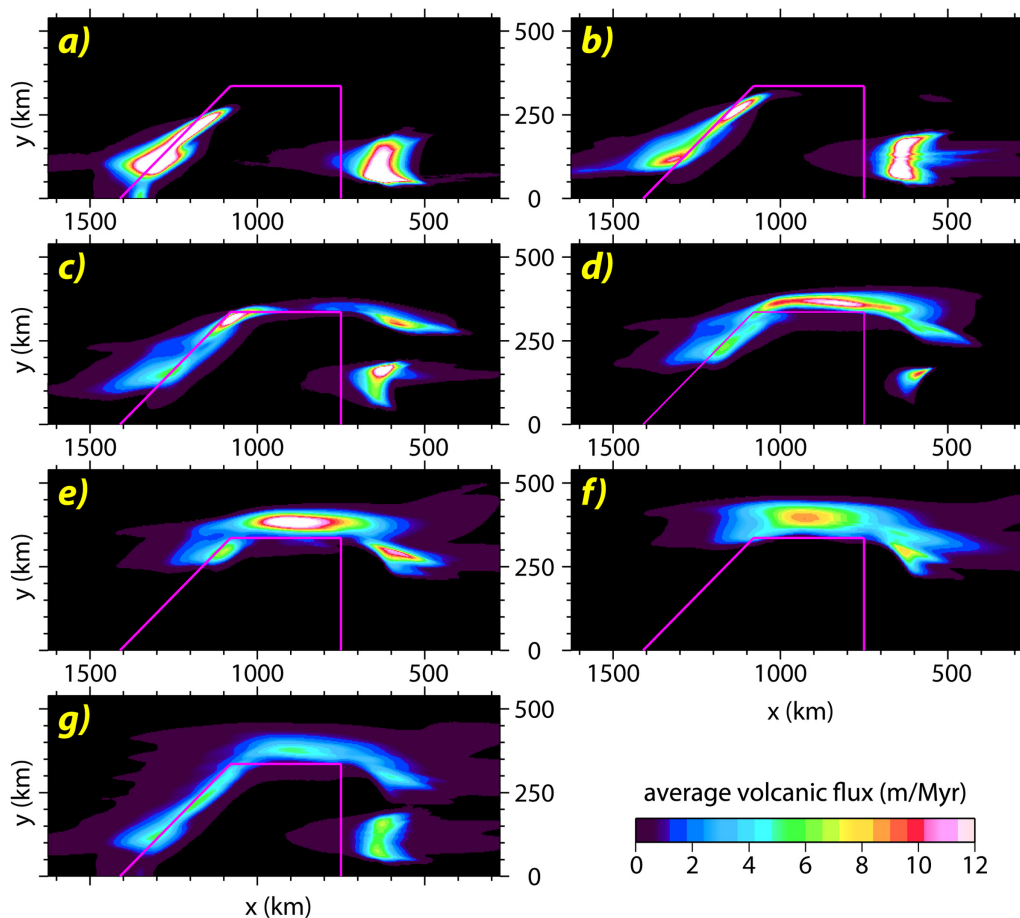


**Figure 8.** Melts extracted from the mantle for cases (a–f) A–F, time-averaged over model times 30–55 Myr. Colors denote average volcanic fluxes per area in m/Myr (or  $\text{m}^3/\text{m}^2/\text{Myr}$ ) with intrusive magmatism or subsequent erosion ignored. The magenta contour outlines the original shape of the plateau. (g) Volcanic fluxes that are not only averaged over time (i.e., 30–55 Myr), but also over cases A–F.

well as  $\eta_p$  between cases E, E1, E2 and E3 (as well as A, A1, A2, A3) while keeping  $\eta_m/\eta_p$  fixed (see Table 2). In addition, we varied  $\eta_m/\eta_p$  between cases E2, E2' and E2'' (as well as A2, A2', and A2''). Figure 9 displays cumulative volcanic fluxes for various cases with different  $\eta_p$  and  $\eta_m$ .

In comparing cases A and A2'' as well as cases E and E2'' (dashed and solid blue lines in Figures 9a and 9b, respectively), we find that decreasing  $\eta_p$  (while keeping  $\eta_m$  fixed) systematically displaces the focus of upwelling toward the edge of the plateau. Moreover, decreasing  $\eta_p$  systematically increases upwelling rates within the pocket, as well as volcanic fluxes. This behavior can be explained by the effects of lower pocket viscosity on TEDC or SDU, or both. TEDC is expected to be boosted by reducing either  $\eta_p$  or  $\eta_m$ , whereas SDU in a low-viscosity pocket is expected to be advanced by higher viscosity ratios  $\eta_m/\eta_p$  — and should be insensitive to the absolute values of  $\eta_p$  or  $\eta_m$ . Thus both mechanisms are fueled as  $\eta_p$  is decreased and  $\eta_m$  is kept fixed.

To distinguish between the two mechanisms, we also compare cases with variable  $\eta_m$  and constant  $\eta_p$ . Increasing  $\eta_m$  while keeping  $\eta_p$  fixed (thereby increasing  $\eta_m/\eta_p$ ) tends to weaken volcanism near the leading edge and alongside of the plateau (blue to red to black solid lines in Figures 9a and 9b). Beyond the far side of the plateau (i.e.,  $x < 750$  km), cumulative volcanic fluxes (i.e., the area beneath the curves) instead increase with increasing  $\eta_m/\eta_p$ . Cumulative fluxes increase as the area of volcanism broadens. Such a behavior indicates that SDU is more efficient in sustaining mantle melting than TEDC beyond the far side of the plateau ( $x < 750$  km), but TEDC is more efficient along the leading edge and sides of the plateau. We note that this analysis cannot distinguish the effect of upwelling due to redirection of shear flow across a step in lithospheric thickness (cf. Figure 2a), which is a variation of SDU that should contribute to volcanism on the plateau's trailing side regardless of the presence of a low-viscosity pocket (and independent of  $\eta_m/\eta_p$ ).

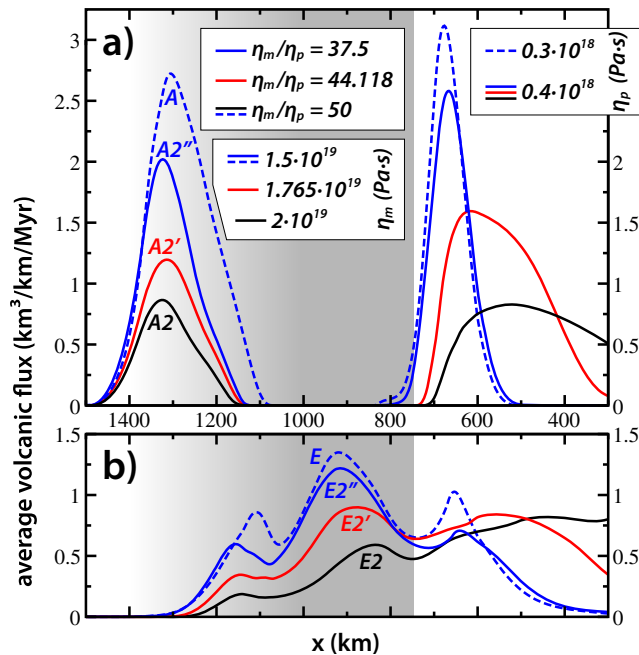


**Figure 9.** Cumulative volcanic flux per km of plate for eight different cases. Volcanic flux is integrated over model times 30–55 Myr, and over the width of the box (i.e., 540 km). For example, the dashed blue lines (in a and b) corresponding to cases A and E are integrations (over  $y$ ) of the melt volumes that are shown in map-view in Figures 8a and 8e, respectively. The area beneath each curve is the total volcanic flux (in  $\text{km}^3/\text{Myr}$ ). Gray shading reflects the original width of the plateau at a given  $x$  (dark gray: 336 km; white: 0 km). (a) Cumulative volcanic flux per km of plate for a subset of cases with  $y_p = 0$  km (A, A2, A2' and A2'') and variable  $\eta_p$ ,  $\eta_m$ , and  $\eta_m/\eta_p$ . (b) Cumulative volcanic flux per km of plate for cases with  $y_p = 277.5$  km (E, E2, E2' and E2'') and variable  $\eta_p$ ,  $\eta_m$ , and  $\eta_m/\eta_p$ .

Increasing (or decreasing) background viscosity  $\eta_m$ , while keeping  $\eta_m/\eta_p$  fixed, is expected to advance SDU relative to TEDC (or vice versa).

#### 4. Discussion and Conclusions

Our numerical experiments show that interaction between viscosity heterogeneity and sublithospheric topography in an environment of horizontal asthenospheric shear flow can sustain upwelling, decompression melting and volcanism. Mantle domains of anomalously low viscosity become displaced and deformed by shear flow. As soon as they approach a step of lithospheric thickness, they critically enhance the local conditions for convective instability, and, in combination with the density jump across the step itself, give rise to vigorous small-scale convection. Such trig-

gered edge-driven convection (TEDC; Figure 2c) provides opportunities for decompression melting as long as the mantle is close to its solidus. In addition, horizontal asthenospheric shear flow directly contributes to upwelling and magmatism. Shear flow is redirected into “shear-driven” upwelling (SDU) as it enters the low-viscosity anomaly (Figure 2b), or as it encounters a lithospheric step, such as that provided by keel of thickened lithosphere (Figure 2a). However, viscosity heterogeneity is critical for upwelling and magmatism on all sides of the keel. In the absence of heterogeneity, upwelling is restricted to only one side and is too weak to sustain decompression melting.

In particular, such asthenospheric upwelling due to a combination of TEDC and SDU can provide an explanation for recent basaltic volcanism surrounding the Colorado Plateau (purple dots in Figure 1 versus Figure 8g). Recent volcanism is focused near the plateau’s margins, has advanced toward the SW side of the plateau [Figure 4 of Crow *et al.*, 2011], and is underlain by seismic low-velocity anomalies. In contrast to the Basin and Range lavas, which are mainly primitive alkali basalts that ascend from their source without significant interaction with the lithosphere [Luhr *et al.*, 1995; Valentine and Perry, 2006; Smith *et al.*, 2008; Muffler *et al.*, 2011], magmatic products along the neighboring side of the Colorado Plateau display a spectrum of compositions ranging from alkalic to calc-alkaline and tholeiitic lavas thus providing evidence for an extended duration of mantle melting and magmatic evolution [Best *et al.*, 1980; Johnsen *et al.*, 2010]. All the above observations are consistent with the predictions of our numerical models, in which hydrous low-viscosity pockets (that should appear seismically slow) exclusively host mantle melting to sustain extensive magmatism along the margins of the plateau (Figure 8g). Model predictions also involve slow encroachment of volcanism onto the side of the plateau that faces asthenospheric shear flow (Figure 7) due to thermomechanical erosion of the sublithospheric keel. The spatiotemporal patterns of mantle upwelling and thermomechanical erosion predicted by our models are moreover qualitatively consistent with observed patterns of recent dynamic uplift that is inferred to be focused along the margins of the Colorado Plateau [Karlstrom *et al.*, 2012], and to have advanced toward its southwestern edge [Crow *et al.*, 2014].

We note however that our simplified geodynamic models are not designed to satisfy all observational constraints at once. For example, our symmetric models cannot account for the occurrence of vigorous volcanism along the southern edge and the absence of volcanism along the northern edge of the Colorado Plateau. Also, our models tend to overpredict the duration of volcanism at any given location (Figure 7) because of the large size of our modeled low-viscosity pockets (our pocket sizes at a given pocket aspect ratio are limited to multiples of model resolution). Accordingly, the observed spatiotemporal patterns of volcanism may be better explained by the presence of multiple small pockets instead of one large pocket, consistent with seismic tomography (Figure 1). The distribution of volcanism implies that pockets tend to travel around the southern edge of the plateau, whereas they tunnel beneath the northern edge, perhaps reflecting differences in pocket initial positions or sublithospheric topography [see *Levander and Miller, 2012*] between the north and south. As low-viscosity pockets give rise to mantle upwelling and exclusively host melting, volcanic patterns may thus directly reflect the viscosity structure of the mantle.

A potential source of low-viscosity material may be related to dehydration of the subducted Farallon slab. Dehydration reactions of serpentine and other hydrous minerals are thought to have hydrated the mantle wedge as far inland as the Colorado Plateau [*Hawkesworth et al., 1993; Dixon et al., 2004*], particularly during a stage of flat subduction associated with the Laramide orogeny [*Coney and Reynolds, 1977; Humphreys et al., 2003*]. Hydration of the mantle wedge may result from percolation of slab-derived fluids [*Li et al., 2008; Sommer et al., 2012*] or the rise of partially molten diapirs of hydrated peridotite [*Gerya and Yuen, 2003*]. Diapirs are predicted to rise close to the subduction zone [*Gerya and Yuen, 2003; Zhu et al., 2009*], and/or further inland where the slab stagnates in the mantle transition zone [*Sigloch et al., 2008; Richard and Bercovici, 2009; Richard and Iwamori, 2010*]. Each of these mechanisms, particularly those involving diapirism, is likely to create strong lateral heterogeneity with hydrous pockets juxtaposed to relatively dry domains. Associated viscosity contrasts of one to two orders of magnitude [cf. *Hirth and Kohlstedt, 1996*] are sufficient for vigorous SDU [*Conrad et al., 2010; Ballmer et al., 2013a*]. Indeed, extensive and variable mantle hydration beneath the western United States is indicated by melt inclusions [*Gazel et al., 2012*] as well as xenolith data [*Li et al., 2008*], and consistent with observations of isostatic adjustment to Pleistocene loads [*Dixon et al., 2004* and references therein] as well as seismic constraints [*Cao and Levander, 2010; Schmandt et al., 2011; Schmandt, 2012*].

Beyond North America, a combination of TEDC and SDU may accordingly be relevant for intraplate volcanism in eastern Asia and Europe, where a long history of subduction is likely to have hydrated the asthenosphere, and where variations in lithospheric thickness are common. Basaltic volcanism in both Southern and Eastern Australia is another candidate as associated with sublithospheric topography at a cratonic margin, as well as vigorous shearing of the asthenosphere [*Demidjuk et al., 2007; Conrad et al., 2011; Davies and Rawlinson, 2014*]. Also, by moving northward, Australia overrides an upper mantle that has likely been hydrated by subduction in Melanesia [*DiCaprio et al., 2011*]. Finally, the Cameroon Volcanic Line in Africa is underlain by a finger-like anomaly of seismically slow mantle that is juxtaposed to a step in lithospheric thickness [*Reusch et al., 2010*]. Vigorous mantle flow in this region is predicted by geodynamic models [*Forte et al., 2010b*] and consistent with seismic-anisotropy measurements [*Koch et al., 2012*]. Shear-driven upwelling, edge-driven convection, or a combination of both mechanisms, may indeed be a viable explanation for many sites of intraplate volcanism globally. Future work will be needed to characterize the roles of asthenospheric shearing, viscosity heterogeneity, and sublithospheric topography for each candidate setting.

#### Acknowledgements

We thank Esteban Gazel, an anonymous reviewer and the editor for their thoughtful and detailed comments that helped to improve the manuscript. This work has been supported by the Nevada Agency of Nuclear Projects, and by NSF grant EAR-1151241 (CPC). A version of the software that was used to run the numerical models (see Methods section) is available at Computational Infrastructure for Geodynamics (<http://www.geodynamics.org>).

#### References

- Ballmer, M. D., J. van Hunen, G. Ito, T. A. Bianco, and P. J. Tackley (2009), Intraplate volcanism with complex age-distance patterns—A case for small-scale sublithospheric convection, *Geochem. Geophys. Geosyst.*, *10*, Q06015, doi:10.1029/2009GC002386.
- Ballmer, M. D., C. P. Conrad, E. I. Smith, and N. Harmon (2013a), Non-hotspot volcano chains produced by migration of shear-driven upwelling toward the East Pacific Rise, *Geology*, *41*(4), 479–482.
- Ballmer, M. D., G. Ito, C. J. Wolfe, and S. C. Solomon (2013b), Double layering of a thermochemical plume in the upper mantle beneath Hawaii, *Earth Planet. Sci. Lett.*, *376*, 155–164.
- Becker, T. W. (2006), On the effect of temperature and strain-rate dependent viscosity on global mantle flow, net rotation, and plate-driving forces, *Geophys. J. Int.*, *167*, 943–957.
- Becker, T. W., V. Schulte-Pelkum, D. K. Blackman, J. B. Kellogg, and R. J. O'Connell (2006), Mantle flow under the western United States from shear wave splitting, *Earth Planet. Sci. Lett.*, *247*(3–4), 235–251.
- Beghein, C., J. A. Snoke, and M. J. Fouch (2010), Depth constraints on azimuthal anisotropy in the Great Basin from Rayleigh-wave phase velocity maps, *Earth Planet. Sci. Lett.*, *289*(3–4), 467–478.

- Best, M. G., E. H. McKee, and P. E. Damon (1980), Space-time-composition patterns of Late Cenozoic Mafic Volcanism, Southwestern Utah and adjoining areas, *Am. J. Sci.*, *280*(10), 1035–1050.
- Bianco, T. A., C. P. Conrad, and E. I. Smith (2011), Time dependence of intraplate volcanism caused by shear-driven upwelling of low-viscosity regions within the asthenosphere, *J. Geophys. Res.*, *116*, B11103, doi:10.1029/2011JB008270.
- Blackwell, D. D., and M. Richards (2004), Geothermal map of North America, Am. Assoc. Petroleum Geologist (AAPG), 1 sheet, scale 1: 6,500,000, Product code 423.
- Camp, V. E., and M. E. Ross (2004), Mantle dynamics and genesis of mafic magmatism in the intermontane Pacific Northwest, *J. Geophys. Res.*, *109*, B08204, doi:10.1029/2003JB002838.
- Cao, A., and A. Levander (2010), High-resolution transition zone structures of the Gorda Slab beneath the western United States: Implication for deep water subduction, *J. Geophys. Res.*, *115*, B07301, doi:10.1029/2009JB006876.
- Christensen, U. (1984), Convection with pressure-dependent and temperature-dependent non-Newtonian rheology, *Geophys. J. R. Astron. Soc.*, *77*(2), 343–384.
- Coney, P. J., and S. J. Reynolds (1977), Cordilleran Benioff zones, *Nature*, *270*(5636), 403–406.
- Conrad, C. P., and M. D. Behn (2010), Constraints on lithosphere net rotation and asthenospheric viscosity from global mantle flow models and seismic anisotropy, *Geochem. Geophys. Geosyst.*, *11*, Q05W05, doi:10.1029/2009GC002970.
- Conrad, C. P., B. Wu, E. I. Smith, T. A. Bianco, and A. Tibbetts (2010), Shear-driven upwelling induced by lateral viscosity variations and asthenospheric shear: A mechanism for intraplate volcanism, *Phys. Earth Planet. Inter.*, *178*(3–4), 162–175.
- Conrad, C. P., T. A. Bianco, E. I. Smith, and P. Wessel (2011), Patterns of intraplate volcanism controlled by asthenospheric shear, *Nat. Geosci.*, *4*(5), 317–321.
- Crow, R., K. Karlstrom, Y. Asmerom, B. Schmandt, V. Polyak, and S. A. DuFrane (2011), Shrinking of the Colorado Plateau via lithospheric mantle erosion: Evidence from Nd and Sr isotopes and geochronology of Neogene basalts, *Geology*, *39*(1), 27–30.
- Crow, R., K. Karlstrom, A. Darling, L. Crossey, V. Polyak, D. Granger, Y. Asmerom, and B. Schmandt (2014), Steady incision of Grand Canyon at the million year timeframe: A case for mantle-driven differential uplift, *Earth Planet. Sci. Lett.*, *397*, 159–173.
- Davies, D. R., and N. Rawlinson (2014), On the origin of recent intraplate volcanism in Australia, *Geology*, doi:10.1130/g36093.1.
- Demidjuk, Z., S. Turner, M. Sandiford, R. George, J. Foden, and M. Etheridge (2007), U-series isotope and geodynamic constraints on mantle melting processes beneath the Newer Volcanic Province in South Australia, *Earth Planet. Sci. Lett.*, *261*(3–4), 517–533.
- DiCaprio, L., M. Gurnis, R. D. Mueller, and E. Tan (2011), Mantle dynamics of continentwide Cenozoic subsidence and tilting of Australia, *Lithosphere*, *3*(5), 311–316.
- Dixon, J. E., T. H. Dixon, D. R. Bell, and R. Malservisi (2004), Lateral variation in upper mantle viscosity: Role of water, *Earth Planet. Sci. Lett.*, *222*, 451–467.
- Forté, A. M., J. X. Mitrovica, R. Moucha, N. A. Simmons, and S. P. Grand (2007), Descent of the ancient Farallon slab drives localized mantle flow below the New Madrid seismic zone, *Geophys. Res. Lett.*, *34*, L04308, doi:10.1029/2006GL027895.
- Forté, A. M., R. Moucha, N. A. Simmons, S. P. Grand, and J. X. Mitrovica (2010a), Deep-mantle contributions to the surface dynamics of the North American continent, *Tectonophysics*, *481*(1–4), 3–15.
- Forté, A. M., S. Quere, R. Moucha, N. A. Simmons, S. P. Grand, J. X. Mitrovica, and D. B. Rowley (2010b), Joint seismic-geodynamic-mineral physical modelling of African geodynamics: A reconciliation of deep-mantle convection with surface geophysical constraints, *Earth Planet. Sci. Lett.*, *295*(3–4), 329–341.
- Gazel, E., T. Plank, D. W. Forsyth, C. Bendersky, C.-T. A. Lee, and E. H. Hauri (2012), Lithosphere versus asthenosphere mantle sources at the Big Pine Volcanic Field, California, *Geochem. Geophys. Geosyst.*, *13*, Q0AK06, doi:10.1029/2012GC004060.
- Gerya, T. V., and D. A. Yuen (2003), Rayleigh-Taylor instabilities from hydration and melting propel 'cold plumes' at subduction zones, *Earth Planet. Sci. Lett.*, *212*(1–2), 47–62.
- Gogus, O. H., and R. N. Pysklywec (2008), Near-surface diagnostics of dripping or delaminating lithosphere, *J. Geophys. Res.*, *113*, B11404, doi:10.1029/2007JB005123.
- Hariç, C., S. Zhong, and F. J. Simons (2010), Constraints on upper mantle viscosity from the flow-induced pressure gradient across the Australian continental keel, *Geochem. Geophys. Geosyst.*, *11*, Q06004, doi:10.1029/2010GC003038.
- Hawkesworth, C. J., K. Gallagher, J. M. Hergt, and F. McDermott (1993), Mantle and slab contributions in arc magmas, *Annu. Rev. Earth Planet. Sci.*, *21*, 175–204.
- Hernlund, J. W., P. J. Tackley, and D. J. Stevenson (2008), Buoyant melting instabilities beneath extending lithosphere: 1. Numerical models, *J. Geophys. Res.*, *113*, B04405, doi:10.1029/2006JB004862.
- Hirth, G. (2002), Laboratory constraints on the rheology of the upper mantle, *Plastic Deformation Minerals Rocks*, *51*, 97–120.
- Hirth, G., and D. L. Kohlstedt (1996), Water in the oceanic upper mantle - Implications for rheology, melt extraction and the evolution of the lithosphere, *Earth Planet. Sci. Lett.*, *144*(1–2), 93–108.
- Huang, J. S., S. J. Zhong, and J. van Hunen (2003), Controls on sublithospheric small-scale convection, *J. Geophys. Res.*, *108*(B8), 2405, doi:10.1029/2003JB002456.
- Humphreys, E., E. Hessler, K. Dueker, C. L. Farmer, E. Erslev, and T. Atwater (2003), How Laramide-age hydration of North American lithosphere by the Farallon slab controlled subsequent activity in the western United States, *Int. Geol. Rev.*, *45*(7), 575–595.
- Johnsen, R., E. I. Smith, and R. Biek (2010), Subalkaline volcanism in the Black Rock Desert and Markagunt Plateau volcanic fields of south-central Utah, edited by S. M. Carney, D. E. Tabet, and C. L. Johnson, in *Geology of South-Central Utah*, *39*, pp. 109–150, Utah Geol. Assoc. Publ.
- Kaislaniemi, L., and J. van Hunen (2014), Dynamics of lithospheric thinning and mantle melting by edge-driven convection: Application to Moroccan Atlas mountains, *Geochem. Geophys. Geosyst.*, *15*, 3175–3189, doi:10.1002/2014GC005414.
- Karato, S. (1986), Does partial melting reduce the creep strength of the upper mantle, *Nature*, *319*(6051), 309–310.
- Karato, S., and P. Wu (1993), Rheology of the upper mantle—A synthesis, *Science*, *260*(5109), 771–778.
- Karlstrom, K. E., et al. (2012), Mantle-driven dynamic uplift of the Rocky Mountains and Colorado Plateau and its surface response: Toward a unified hypothesis, *Lithosphere*, *4*(1), 3–22.
- Katz, R. F., M. Spiegelman, and C. H. Langmuir (2003), A new parameterization of hydrous mantle melting, *Geochem. Geophys. Geosyst.*, *4*(9), 1073, doi:10.1029/2002GC000433.
- King, S. D., and D. L. Anderson (1998), Edge-driven convection, *Earth Planet. Sci. Lett.*, *160*(3–4), 289–296.
- Koch, F. W., D. A. Wiens, A. A. Nyblade, P. J. Shore, R. Tibi, B. Ateba, C. T. Tabod, and J. M. Nnange (2012), Upper-mantle anisotropy beneath the Cameroon Volcanic Line and Congo Craton from shear wave splitting measurements, *Geophys. J. Int.*, *190*(1), 75–86.
- Kohlstedt, D. L., and M. E. Zimmerman (1996), Rheology of partially molten mantle rocks, *Annu. Rev. Earth Planet. Sci.*, *24*, 41–62.

- Le Pourhiet, L., M. Gurnis, and J. Saleeby (2006), Mantle instability beneath the Sierra Nevada mountains in California and Death Valley extension, *Earth Planet. Sci. Lett.*, *251*(1-2), 104–119.
- Levander, A., and M. S. Miller (2012), Evolutionary aspects of lithosphere discontinuity structure in the western US, *Geochem. Geophys. Geosyst.*, *13*, Q0AK07, doi:10.1029/2012GC004056.
- Levander, A., B. Schmandt, M. S. Miller, K. Liu, K. E. Karlstrom, R. S. Crow, C. T. A. Lee, and E. D. Humphreys (2011), Continuing Colorado plateau uplift by delamination-style convective lithospheric downwelling, *Nature*, *472*(7344), 461–465.
- Li, Z.-X. A., C.-T. A. Lee, A. H. Peslier, A. Lenardic, and S. J. Mackwell (2008), Water contents in mantle xenoliths from the Colorado Plateau and vicinity: Implications for the mantle rheology and hydration-induced thinning of continental lithosphere, *J. Geophys. Res.*, *113*, B09210, doi:10.1029/2007JB005540.
- Liu, L., and D. R. Stegman (2012), Origin of Columbia River flood basalt controlled by propagating rupture of the Farallon slab, *Nature*, *482*(7385), 386–389.
- Luhr, J. F., J. J. Aranda-Gomez, and T. B. Housh (1995), San-Quintin Volcanic Field, Baja-California-Norte, Mexico - Geology, Petrology, and Geochemistry, *J. Geophys. Res.*, *100*(B6), 10,353–10,380.
- Moresi, L., S. J. Zhong, and M. Gurnis (1996), The accuracy of finite element solutions of Stokes' flow with strongly varying viscosity, *Phys. Earth Planet. Inter.*, *97*(1-4), 83–94.
- Muffler, L. J. P., M. A. Clyne, A. T. Calvert, and D. E. Champion (2011), Diverse, discrete, mantle-derived batches of basalt erupted along a short normal fault zone: The Poison Lake chain, southernmost Cascades, *Geol. Soc. Am. Bull.*, *123*(11-12), 2177–2200.
- Nelson, S. T., and D. G. Tingey (1997), Time-transgressive and extension-related basaltic volcanism in southwest Utah and vicinity, *Geol. Soc. Am. Bull.*, *109*(10), 1249–1265.
- Obrebski, M., R. M. Allen, M. Xue, and S.-H. Hung (2010), Slab-plume interaction beneath the Pacific Northwest, *Geophys. Res. Lett.*, *37*, L14305, doi:10.1029/2010GL043489.
- Reid, M. R., R. A. Bouchet, J. Blichert-Toft, A. Levander, K. Liu, M. S. Miller, and F. C. Ramos (2012), Melting under the Colorado Plateau, USA, *Geology*, *40*(5), 387–390.
- Reusch, A. M., A. A. Nyblade, D. A. Wiens, P. J. Shore, B. Ateba, C. T. Tabod, and J. M. Nnange (2010), Upper mantle structure beneath Cameroon from body wave tomography and the origin of the Cameroon Volcanic Line, *Geochem. Geophys. Geosyst.*, *11*, Q10W07, doi:10.1029/2010GC003200.
- Richard, G. C., and D. Bercovici (2009), Water-induced convection in the Earth's mantle transition zone, *J. Geophys. Res.*, *114*, B01205, doi:10.1029/2008JB005734.
- Richard, G. C., and H. Iwamori (2010), Stagnant slab, wet plumes and Cenozoic volcanism in East Asia, *Phys. Earth Planet. Inter.*, *183*(1-2), 280–287.
- Richter, F. M., and B. Parsons (1975), On the interaction of two scales of convection in the mantle, *J. Geophys. Res.*, *80*(17), 2529–2541.
- Rowley, P. D., C. G. Cunningham, T. A. Steven, H. H. Mehnert, and C. W. Naeser (1997), Igneous and tectonic setting of the Marysvale Volcanic Field and its relation to other igneous centers in Utah and Nevada, in *Proceedings on Laccolith Complexes of Southeastern Utah: Time of Emplacement and Tectonic Setting*, U.S. Geol. Surv. Bull. 2158, edited by J. D. Friedman and A. C. Huffman, 292 pp. U.S. Govern. Print. Off., Washington, D. C.
- Roy, M., T. H. Jordan, and J. Pederson (2009), Colorado Plateau magmatism and uplift by warming of heterogeneous lithosphere, *Nature*, *459*(7249), 978–982.
- Schmandt, B. (2012), Mantle transition zone shear velocity gradients beneath USArray, *Earth Planet. Sci. Lett.*, *355*, 119–130.
- Schmandt, B., and E. Humphreys (2010), Complex subduction and small-scale convection revealed by body-wave tomography of the western United States upper mantle, *Earth Planet. Sci. Lett.*, *297*(3-4), 435–445.
- Schmandt, B., K. G. Dueker, S. M. Hansen, J. J. Jasbinsek, and Z. Zhang (2011), A sporadic low-velocity layer atop the western US mantle transition zone and short-wavelength variations in transition zone discontinuities, *Geochem. Geophys. Geosyst.*, *12*, Q08014, doi:10.1029/2011GC003668.
- Sigloch, K., N. McQuarrie, and G. Nolet (2008), Two-stage subduction history under North America inferred from multiple-frequency tomography, *Nat. Geosci.*, *1*(7), 458–462.
- Smith, I. E. M., S. Blake, C. J. N. Wilson, and B. F. Houghton (2008), Deep-seated fractionation during the rise of a small-volume basalt magma batch: Crater Hill, Auckland, New Zealand, *Contrib. Mineral. Petrol.*, *155*(4), 511–527.
- Smith, R. B., M. Jordan, B. Steinberger, C. M. Puskas, J. Farrell, G. P. Waite, S. Husen, W.-L. Chang, and R. O'Connell (2009), Geodynamics of the Yellowstone hotspot and mantle plume: Seismic and GPS imaging, kinematics, and mantle flow, *J. Volcanol. Geotherm. Res.*, *188*(1-3), 26–56.
- Sommer, H., K. Regenauer-Lieb, B. Gasharova, and H. Jung (2012), The formation of volcanic centers at the Colorado Plateau as a result of the passage of aqueous fluid through the oceanic lithosphere and the subcontinental mantle: New implications for the planetary water cycle in the western United States, *J. Geodyn.*, *61*, 154–171.
- Sonder, L. J., and C. H. Jones (1999), Western United States extension: How the West was widened, *Annu. Rev. Earth Planet. Sci.*, *27*, 417–462.
- Till, C. B., L. T. Elkins-Tanton, and K. M. Fischer (2010), A mechanism for low-extent melts at the lithosphere-asthenosphere boundary, *Geochem. Geophys. Geosyst.*, *11*, Q10015, doi:10.1029/2010GC003234.
- Valentine, G. A., and N. Hirano (2010), Mechanisms of low-flux intraplate volcanic fields-Basin and Range (North America) and northwest Pacific Ocean, *Geology*, *38*(1), 55–58.
- Valentine, G. A., and F. V. Perry (2006), Decreasing magmatic footprints of individual volcanoes in a waning basaltic field, *Geophys. Res. Lett.*, *33*, L14305, doi:10.1029/2006GL026743.
- van Wijk, J., J. van Hunen, and S. Goes (2008), Small-scale convection during continental rifting: Evidence from the Rio Grande rift, *Geology*, *36*(7), 575–578.
- van Wijk, J. W., W. S. Baldrige, J. van Hunen, S. Goes, R. Aster, D. D. Coblenz, S. P. Grand, and J. Ni (2010), Small-scale convection at the edge of the Colorado Plateau: Implications for topography, magmatism, and evolution of Proterozoic lithosphere, *Geology*, *38*(7), 611–614.
- West, J. D., M. J. Fouch, J. B. Roth, and L. T. Elkins-Tanton (2009), Vertical mantle flow associated with a lithospheric drip beneath the Great Basin, *Nat. Geosci.*, *2*(6), 438–443.
- Yuan, H., and B. Romanowicz (2010), Depth dependent azimuthal anisotropy in the western US upper mantle, *Earth Planet. Sci. Lett.*, *300*(3-4), 385–394.
- Zhong, S., M. T. Zuber, L. Moresi, and M. Gurnis (2000), Role of temperature-dependent viscosity and surface plates in spherical shell models of mantle convection, *J. Geophys. Res.*, *105*(B5), 11,063–11,082.
- Zhu, G., T. V. Gerya, D. A. Yuen, S. Honda, T. Yoshida, and J. A. D. Connolly (2009), Three-dimensional dynamics of hydrous thermal-chemical plumes in oceanic subduction zones, *Geochem. Geophys. Geosyst.*, *10*, Q11006, doi:10.1029/2009GC002625.
- Zou, H. B. (1998), Trace element fractionation during modal and nonmodal dynamic melting and open-system melting: A mathematical treatment, *Geochem. Cosmochem. Acta*, *62*(11), 1937–1945.